IEEE Access
Multidisciplinary | Rapid Review | Open Access Journal

Received 1 September 2023, accepted 24 September 2023, date of publication 2 October 2023, date of current version 10 October 2023.

Digital Object Identifier 10.1109/ACCESS.2023.3321545

RESEARCH ARTICLE

Real-Time Localization Method of Large Pressure Vessel Leaks Based on Improved CNN and STCA of Elastic Wavefield

BIAN XU[1,2] AND HUANG XINJING[2]

[1]Tianjin Ren'ai College, Tianjin 301636, China
[2]State Key Laboratory of Precision Measurement Technology and Instruments, Tianjin University, Tianjin 300072, China

Corresponding author: Huang Xinjing (huangxinjing@tju.edu.cn)

This work was supported in part by the Scientific Research Program of Tianjin Municipal Education Commission under Grant 2019kj150, and in part by Tianjin University under Grant FZ221003.

ABSTRACT In this paper, a real-time leak source localization method based on convolutional neural network (CNN) of elastic wavefield images and spatio-temporal correlation analysis (STCA) is developed for the pressure vessel leakage. This method uses a single sensor array coupled to the wall to collect the elastic wave data excited by the leak source. Besides, the distance R and the direction θ between the leak source and the sensor array are calculated based on CNN and STCA respectively, to finally obtain the location (R, θ) of the leak source. In this paper, the digital twin model of the experimental platform is established, the training set is obtained by the finite element simulation, and the CNN model applied to the elastic wavefield images is studied and constructed. The experimental results show that the maximum locating error is 1.46 cm and the average locating error is about 0.56 cm within the range of a 1 m^2 experimental plate based on the method proposed in this paper.

INDEX TERMS Elastic wave, leakage, location, sensor array, deep learning.

I. INTRODUCTION

Pressure vessel walls are under pressure at any time, once a leak occurs, the pressure difference between two sides of the wall will lead to fluid (gas, liquid) quickly to low pressure flow [1], which will not only bring huge economic losses and energy waste, but also could cause explosions and other malignant accidents. Therefore, it is necessary to monitor and locate the leak source in real time.

For the leakage of large pressure vessels, such as spacecraft, manual detection methods such as CTRL system [2] or helium mass spectrometer system [3] are often used to locate the leakage. Nevertheless, this method cannot achieve real-time localization [4]. In consequence, it is not suitable for leak detection in large vessels such as spacecraft, and has poor localization accuracy due to the introduction of manual labor. In addition, another method that detects and locates the source of the leakage using the acoustic emission signal excited when the leak is generated, such as the UltraWIS system [5], which is also been applied to pipeline gas leak detection successfully [6], [7], structural health monitoring [8], pressure vessel leakage locating [9] and other fields. Each method has high locating accuracy, good real-time performance, and a relatively simple system. However, in practical applications, they need to accurately detect the data at the time of leaks, which has limitations. Namely it is mainly suitable for detecting sound sources with significant characteristics in the time-frequency domain. To solve the above problems, the researchers have increased the data dimension [10], and enhanced the spatial sampling rate of the data, so as to obtain some achievements. Reusser et al. [11] proposed the application of multiple 8 × 8 square sensor arrays to locate the leakage signal. This method calculated the intensity distribution of the wave number domain in the leakage which was excited in the medium in the sensor array, and obtained the maximum value direction in the wave number domain, thereby obtained the leakage source location information. Aiming at existing leakage sources, Bian et al. [12], [13] proposed a leakage source location method by studying the spatio-temporal correlation of leak-excited elastic waves.

The associate editor coordinating the review of this manuscript and approving it for publication was Santi C. Pavone.

This kind of methods expanded the scope of application of the locating method through the study on the spatial distribution of sound wave excited by leakage in the wall, so it can locate the leakage source at any stage of the leakage, which improved the accuracy and stability of the location, whereas, it increased the complexity and cost of the location method and reduced the practicability and real-time performance in the meantime.

For some complex application scenarios, which could bring a large number of parameters, the research method based on wave field mathematical model has some limitations [14], [15]. Based on this situation, many scholars have conducted lots of research work using machine learning techniques which is already applied successfully in many other flied [16], [17], [18], and achieved good results in different fields. Deo and Jaiman [19] presented a deep learning technique for data-driven predictions of wave propagating in a fluid medium. The technique relied on an attention-based convolutional recurrent autoencoder network. Spandonidis et al. [20] discussed and evaluated the effectiveness of deep learning methods for oil and gas pipeline leak detection based on wireless sensor networks. Wu and Lee [21] used an improved multilayer perceptron neural network to achieve leak localization for gas pipelines. Ye and Toyama [22] proposed automatic defect detection for ultrasonic wave propagation imaging method using spatio-temporal convolution neural networks. Wang et al. [23] proposed a rapid guided wave imaging method based on CNN to quantitatively evaluate the corrosion damage. Cui et al. [24] had similar work for the skin-stringer composite aircraft panel. To meet the needs of real-time orbital structural health monitoring, Mahajan and Banerjee [25] proposed an acoustic emission source location method based on deep learning. Haiqiang et al. [26], in collaboration with colleagues from the University of California, proposed a machine learning-based passive localization method for underwater sound sources, which achieved high accuracy underwater sound source localization without relying on theoretical modeling of underwater sound fields.

In summary, the existing research work cannot fully require the strict requirements of large pressure vessels leakage localization on the complexity and the real-time performance of the localization system. Apart from the previous approached, according to the practical application requirements, based on the deep learning, this paper proposes a leakage localization method which uses a single sensor array coupled to the wall to collect the elastic wave data excited by the leak source. Besides, the distance R and the direction θ between the leak source and the sensor array are calculated based on CNN and STCA respectively, so as to finally obtain the location (R, θ) of the leak source. Compared with the existing methods, this method has the advantages of simple structure, low system cost, easy implementation, and universality, which can satisfy the requirements of most of the conditions of the large pressure vessel leakage in real time and accurate location.

II. LOCATING PRINCIPLE

The continuous gas leakage of the pressure vessel is a complex phenomenon, and any tiny initial difference or disturbance will cause significant parameter changes in the leakage process [27], it is difficult to build an accurate mathematical model that could apply to a wide range of situations. According to the theory of gas dynamics and acoustics, once a gas leak occurs in a pressure vessel, firstly, the high-speed gas flows from the leak (inflow) to form a turbulent jet, which leads to irregular gas motion and excites a large number of random acoustic signals [28]; secondly, the elastic waves excited by the leak in the vessel wall propagate in the form of Lamb waves [29], and this type of wave propagation has a significant dispersion phenomenon; finally, the complex structure of the vessel wall has a complex effect on the propagation of the elastic waves excited in the wall. The above situation makes the vibration signal acquire on the vessel wall randomly in the time domain, and its randomness is weaker than the white noise that close to the background noise, which is difficult to obtain the locations of leakage sources.

Based on the characteristics of elastic waves excited by leakage in the wall, and combining with the field experimental data, this paper achieves the simulation of the elastic wave field excited by the leakage in the vessel wall using finite elements, obtains a large amount of training sample data, establishes a deep learning model, and successfully realizes the real-time localization of the leakage source. The locating schematic is shown in Fig. 1. Compared to traditional methods, this method significantly reduces the complexity of the system, allows and realizes real-time localization of the leak source using a single sensor array. Meanwhile, it can decrease the amount of data to be processed in the field, and make the method more applicable.

Based on polar coordinate system, localization can be obtained by calculating the angle θ and the distance R. Elastic wave field data acquisition model is shown in Fig. 2.

Let F(t) represent the elastic wave excited by the leakage source propagating in the wall, A represents the signal amplitude, f represents the signal frequency, and the frequency range is (f_a, f_b). Based on the wave equation, F(t) can be written as (1).

$$F(t) = \int_{f_a}^{f_b} A \cdot \exp(2j\pi f \cdot t) df \tag{1}$$

As shown in Fig. 2, R_i represents the distance between the i-th sensor in the array and the leakage source, $(i = 1, 2, \ldots, N, \ldots, N + m)$, α_i represents the attenuation coefficient of signal. Since the elastic wave propagates in the form of a Lamb wave in the thin plate, there is an obvious dispersion phenomenon. According to the theoretical derivation and the basis of previous work [12], the signal received by the sensor is mainly A_0 mode under the conditions of the frequency band and plate thickness involved, the other modes can be ignored. let c(f) represent the propagation velocity of

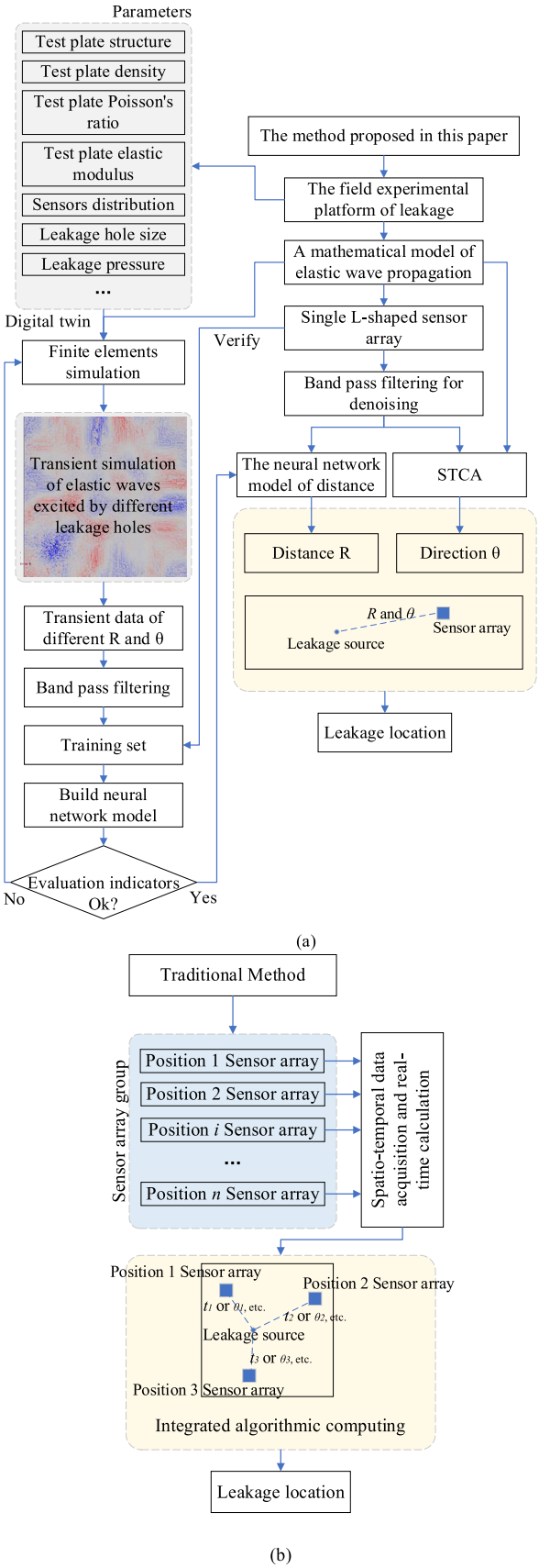

FIGURE 1. locating schematic (a. The method proposed in this paper; b. Traditional Method).

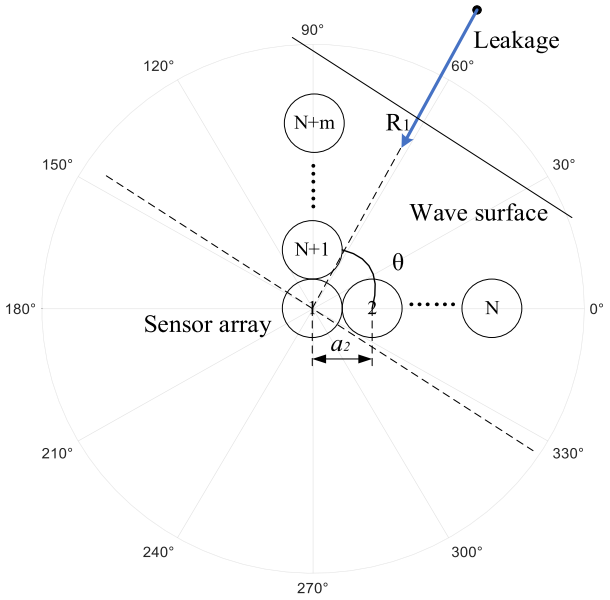

FIGURE 2. Elastic wave field data acquisition model.

the elastic wave in A_0 mode when the frequency is f. Let k represent the wave number $k = \frac{2\pi f}{c(f)}$.

The data which are collected by the i-th sensor in the array could be shown as (2).

$$s_i(t) = \int_{f_a}^{f_b} \alpha_i \cdot A \cdot \exp(2j\pi f \cdot t + jkR_i)df \tag{2}$$

A. CALCULATE THE DIRECTION PARAMETER θ WITH STCA

Let a_i represent the distance between the i-th array element and the reference array element (No. 1 array element is selected in this paper), let θ represent the angle between the leakage source and the sensor array reference line as show in Fig. 2. In general, the sensor array size is much less than the distance between the leak source and the sensor array (the difference value is usually more than an order of magnitude), that is $R_i \gg a_i$, the wave surface covered by the sensor array can be approximated as a plane, so R_i can be approximated as (3).

$$\begin{aligned} R_i &= R_1 + a_i \cdot Q_i(\theta) \\ Q_i(\theta) &= \begin{cases} 0 & i = 1 \\ \cos\theta & i = 2, \cdots, N \\ \sin\theta & i = N+1, N+2, \cdots N+m \end{cases} \end{aligned} \tag{3}$$

Then, according to (2) and (3), $s_i(t)$ can also be expressed as

$$s_i(t) = \int_{f_a}^{f_b} \alpha_i \cdot A \cdot \exp\left[2j\pi f \cdot t + jkR_1 + jka_iQ_i(\theta)\right]df \tag{4}$$

The sensor array matrix acquisition data is represented in matrix form as **S**:

$$\mathbf{S} = [S_1(t), S_2(t), \cdots, S_{N+m}(t)] \tag{5}$$

Let β represent the estimated direction and construct the matrix **U**:

$$\mathbf{U} = \begin{bmatrix} 1 \\ \exp\left[-jka_2Q_2\left(\beta\right)\right] \\ \exp\left[-jka_3Q_3\left(\beta\right)\right] \\ \vdots \\ \exp\left[-jka_{N+m}Q_{N+m}\left(\beta\right)\right] \end{bmatrix} \tag{6}$$

In the time window (t_c, t_d), let

$$\mathrm{E} = \int_{t_c}^{t_d} (\mathbf{S} \times \mathbf{U})\, dt \tag{7}$$

Let:

$$\begin{cases} q_h = jk \cdot a_i[\cos(\theta) - \cos(\beta)] \\ q_v = jk \cdot a_i[\sin(\theta) - \sin(\beta)] \end{cases} \tag{8}$$

The distance among each sensor of the array is very small, thus neglecting the differences of α_i, assuming $\alpha = \alpha_i$, then (7) can be expanded as:

$$E = \alpha \cdot \int_{t_a}^{t_b} \int_{f_0}^{f_n} S_1(t) \cdot \left\{ \sum_{i=1}^{N} e^{q_h} + \sum_{i=N+1}^{N+m} e^{q_v} \right\} dfdt \tag{9}$$

In practical application, the distance between sensors is generally equal, that is

$$a_i = \begin{cases} 0 & i = 1 \\ i \cdot a_2 & i = 2, \cdots, N \\ (N-i) \cdot a_2 & i = N+1, N+2, \cdots N+m \end{cases} \tag{10}$$

According to the properties of geometric progression and Euler's formula, (9) can be written as:

$$E = \alpha \cdot \int_{t_a}^{t_b} \int_{f_0}^{f_n} S_1(t) \cdot \left\{ e^{\left(-N-\frac{1}{2}\right)q_h} \cdot \frac{\sin(N \cdot q_h)}{\sin(q_h)} + e^{\left(-m-\frac{1}{2}\right)q_v} \cdot \frac{\sin(N \cdot q_v)}{\sin(q_v)} \right\} dfdt \tag{11}$$

According to the property of function $\frac{\sin(n \cdot x)}{\sin(x)}$ and e^x, E reaches the maximum when both q_h and q_v are zero, meanwhile, based on the (8), $\beta = \theta, \beta \in (0°, 90°)$ could be obtained. The E-β relationship calculated in the actual experiment is shown in Fig. 3.

The experimental results show that the leakage excitation in the wall is a broadband signal (as show in Fig.4), and the ambient noise coupled to the wall is concentrated in the low frequency region below 200KHz [12], so the bandpass filtering is used to ensure the signal-to-noise ratio of the data during calculating. (The f range is usually taken as [200kHz,600kHz]). Meanwhile, in order to solve the velocity c error caused by dispersion, the above f-range is usually divided into narrower frequency bands (with less velocity variation) in the calculation. Furthermore, the final results can be obtained by combining the results of multiple frequency bands. The angle value corresponding to the largest peak in the curve is the true angle between the leak source and the sensor array.

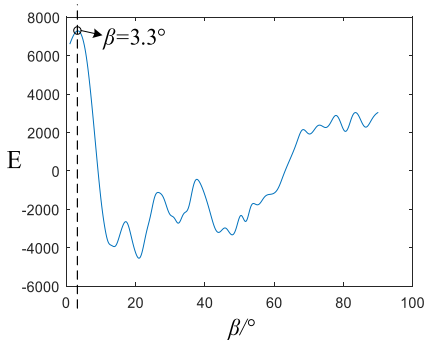

FIGURE 3. E-β relationship curve.

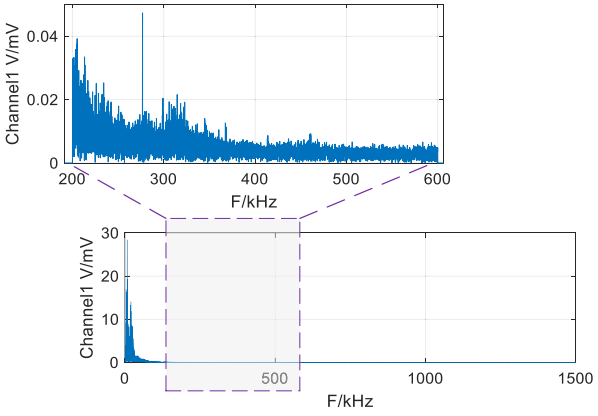

FIGURE 4. The spectrum of elastic wave excited by leakage.

B. CALCULATE THE DISTANCE PARAMETER R WITH CNN

The elastic wave excited by leakage has the following characteristics. For one thing, its amplitude is very random in the time domain due to the perturbation of external influences, thus it is difficult to establish accurate mathematical models; For another, it is difficult to analyze the wave field distribution characteristics after the elastic waves are superimposed by the wall structure in several times. Therefore, based on the above factors, an enhanced approach for obtaining the distance parameter R by using deep learning in this work.

1) DATASET CONSTRUCTION

According to the propagation theory of Lamb waves, the spatial energy distribution of elastic waves in the vessel wall is influenced by the propagation distance, refer to (4). Meanwhile, the dispersion phenomenon makes the elastic wave field formed in space after the elastic wave propagates for a certain time closely related to the collection location and

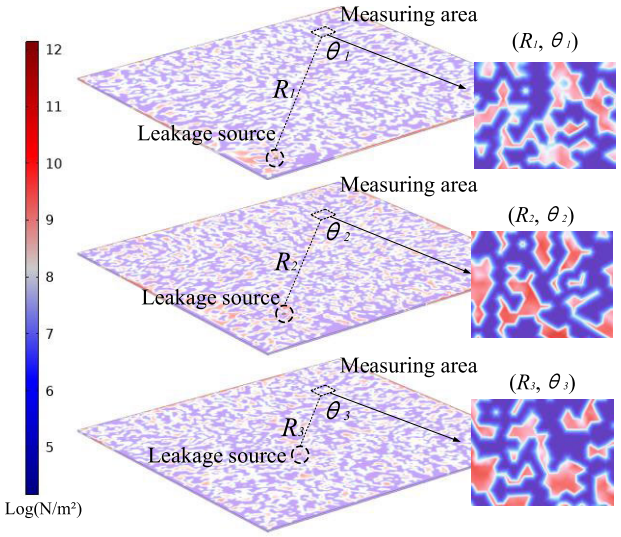

FIGURE 5. Transient diagram of finite element simulation of leakage at different positions.

the leakage location. The finite element simulation of the elastic wave field is carried out, and the transient simulation results of Z-axis stress tensor in the same moment after the leakage occurred at different locations are obtained, as shown in Fig. 5.

In order to obtain the spatial and temporal domain data of the elastic wave field excited by the leakage source at the distance R, this paper uses an L-type sensor array, as shown in (5). Taking the 8-element L-shaped sensor array as an example (sampling point spacing is 8mm), the data obtained from it is shown in Fig. 6.

The $s_i(t)$ is cut at equal intervals in the time domain and divided into a total of l segments, let w represent the number of sampling points contained in the time segment, and according to (2), the data of the x-th time segment can be written as $s_i(t_x)$. In order to fully learn the spatial and temporal domain features of the leaking excited elastic waves, the sensor array acquisition data is constructed as a 3D matrix form to be used as a deep learning model input. For a certain angle θ and distance R, the data collected by $N + m$ elements in the array are formed into a sample data, which is denoted as $\mathrm{I}_{R,\theta}$. Additionally, $\mathrm{I}_{R,\theta}$ can be expressed as:

$$\mathbf{I}_{R,\theta} = \begin{matrix} x=1 \\ \\ \\ \\ \end{matrix} \begin{bmatrix} s_1(t_1) & s_1(t_2) & \cdots & s_1(t_l) \\ s_2(t_1) & s_2(t_2) & \cdots & s_2(t_l) \\ \vdots & \vdots & & \vdots \\ s_{N+m}(t_1) & s_{N+m}(t_2) & \cdots & s_{N+m}(t_l) \end{bmatrix} \begin{matrix} x=2 \\ \\ \\ \\ \end{matrix} \cdots \begin{matrix} x=l \\ \\ \\ \\ \end{matrix} \tag{12}$$

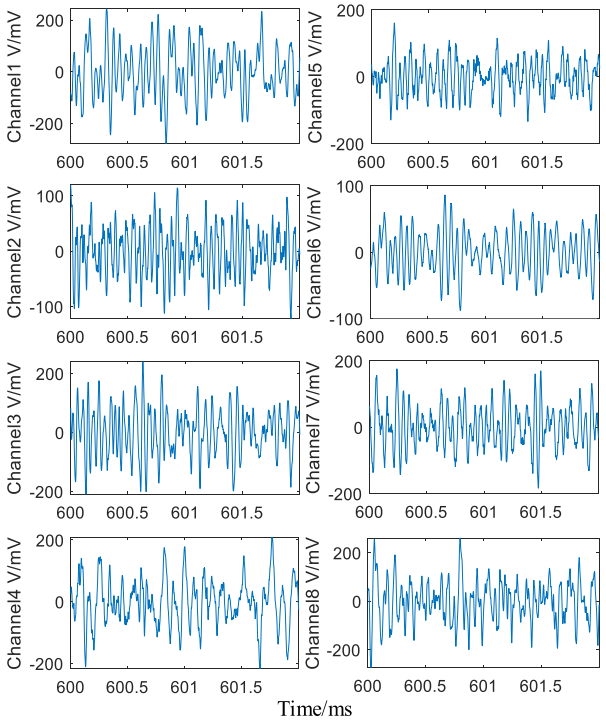

FIGURE 6. Elastic wave data collected by an 8-element L-shaped sensor array.

Through finite element simulation and field experiments, $\mathrm{I}_{R,\theta}$ at different distances R and angles θ are obtained to construct a training data set to meet the needs of deep learning.

2) DEEP LEARNING NETWORK DESIGN

According to (12), the input data can be viewed as a two-dimensional array of amplitudes in the Spatio-temporal coordinate system, in order to solve the problem of extremely unbalanced sampling rate of time dimension and space dimension when actually acquiring the data, and satisfy the deep learning requirement of this kind of data, this paper proposes a convolutional neural network model based on rectangular convolution kernel (abbreviated as RecCNN). This model can better perceive and learn the time-domain features of different sampling points without increasing the depth of the model. The main structure of the designed network is shown as Fig. 7.

As shown in Fig. 7, the network model uses six convolutional layers (Conv), six batch Normalization Layers (BN), a maximum pooling layer (Max-pool), an average pooling layer (Aver-pool), three fully connected layers (FC), and the RELU activation function to avoid the problem of gradient disappearance [30], the calculation formula is shown in (13).

$$RELU(Z) = \begin{cases} Z & Z \geqslant 0 \\ 0 & Z < 0 \end{cases} \tag{13}$$

The mean square error (RMSE), mean Square Error (MSE), mean absolute error (MAE), R-square(R^2), Nash-Sutcliffe Efficiency (NSE) and RMSE-observations standard

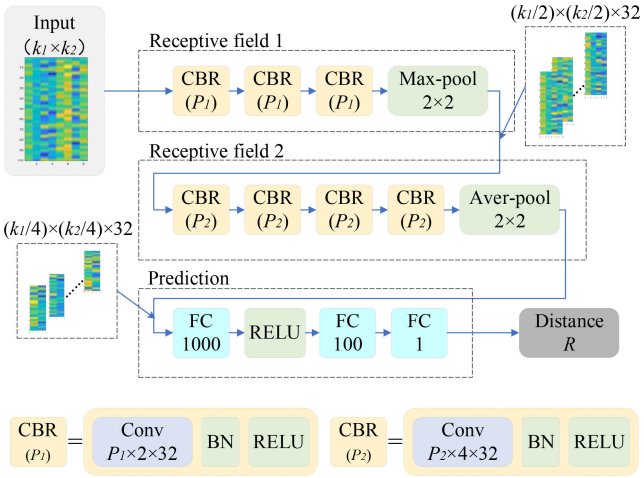

FIGURE 7. The main structure of the CNN model.

deviation ratio (RSR) are used as evaluation indicators to evaluate the measurement results [31], [32]. Let Q represent the total number of samples, g_j represent the actual distance value of the j-th sample, and $\bar{g}$ represent its mean; y_j represent the distance prediction value of the j-th sample, y_j^{pred} represent the distance prediction for the j-th sample outside the training set, then RMSE, MAE, R^2, NSE and RSR can be expressed respectively as shown in (14)-(19).

$$RMSE = \sqrt{\frac{1}{Q}\sum_{j=1}^{Q}(g_j - y_j)^2} \tag{14}$$

$$MSE = \frac{1}{Q}\sum_{j=1}^{Q}(g_j - y_j)^2 \tag{15}$$

$$MAE = \frac{1}{Q}\sum_{j=1}^{Q}\left|g_j - y_j\right| \tag{16}$$

$$R^2 = 1 - \frac{\sum_{j=1}^{Q}\left(g_j - y_j\right)^2}{\sum_{j=1}^{Q}\left(g_j - \bar{g}\right)^2} \tag{17}$$

$$NSE = 1 - \frac{\sum_{j=1}^{Q}\left(g_j - y_j^{pred}\right)^2}{\sum_{j=1}^{Q}\left(g_j - \bar{g}\right)^2} \tag{18}$$

$$RSR = \frac{\sqrt{\sum_{j=1}^{Q}\left(g_j - y_j\right)^2}}{\sqrt{\sum_{j=1}^{Q}\left(g_j - \bar{g}\right)^2}} \tag{19}$$

III. SAMPLE ACQUISITION AND CNN TRAINING

According to the deep learning method, the calculation of the distance R is mainly divided into two stages: training and prediction. The main steps of the method in this paper are shown in Fig. 8.

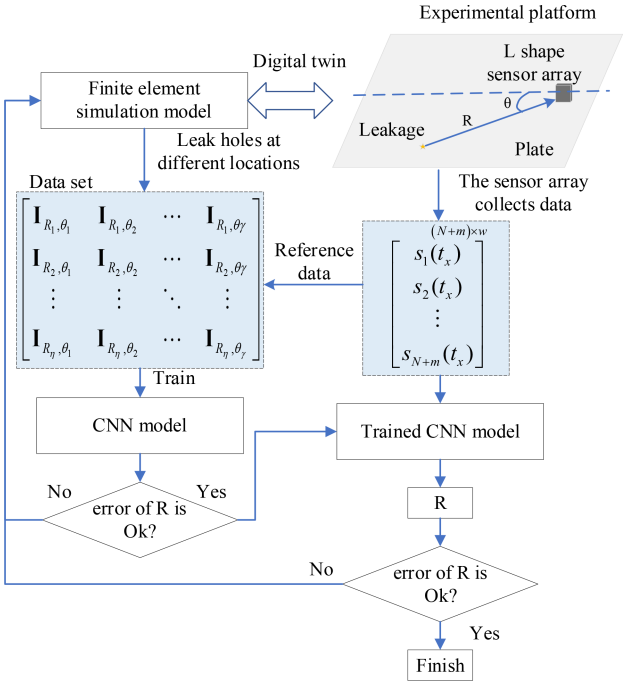

FIGURE 8. Distance R calculation flow chart.

A. DIGITAL TWIN-BASED DATASET CONSTRUCTION

Since it is difficult to obtain a large amount of sample data from different locations through experiments, this paper uses finite element simulation to simulate leaks in order to obtain sufficient sample data for training. For the purpose of providing reasonable parameters for the simulation model, an experimental platform for simulating pressure vessel leakage is designed and implemented, and the elastic wave data excited by the leakage in the wall are collected by sensor arrays. The main components of the experimental platform are shown in Fig. 9.

The experimental plate is machined into a flat plate (length and width of 1 m×1 m, thickness of 2.5 mm) using the same 5A06 magnesium aluminum alloy to simulate the pressure vessel wall. The plate is pre-drilled with circular through-holes of 1mm diameter at different positions, and a vacuum pump is connected to a vacuum nozzle to provide air pressure difference to simulate the gas leakage. A sensor array is coupled to the experimental plate to measure the vertical vibration caused by elastic waves excited by the leakage. Eight nano30 sensors of PAC (Physical Acoustics Corporation, USA) are used as elements to form an L-shaped sensor array connected to a preamplifier (40 dB gain). The amplifier amplifies the signal from the element and transmits them to the acoustic emission instrument. The instrument (fully digital 16-channel acoustic emission detection system DS2-16A) processes the data collected from the multiple

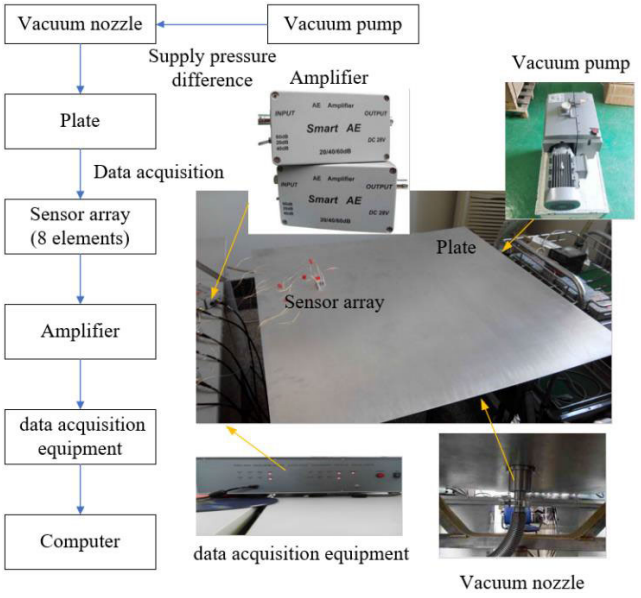

FIGURE 9. The experimental platform.

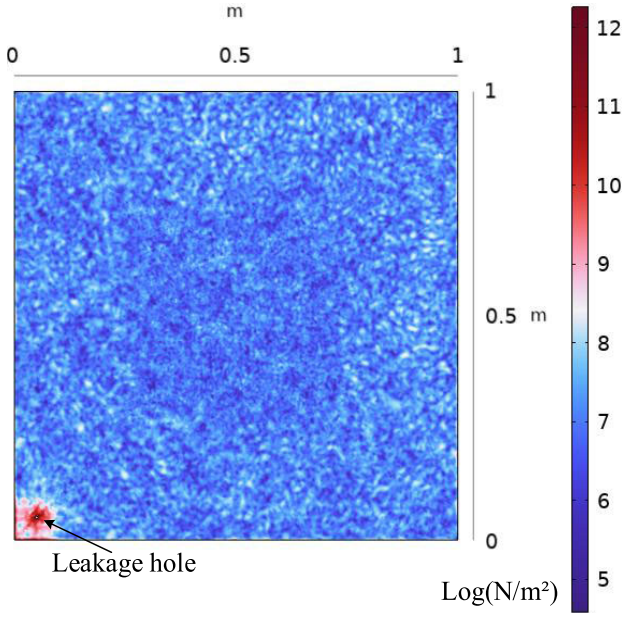

FIGURE 10. Transient diagram of elastic wave propagation (Logarithm of the stress tensor in the Z-direction).

channels and transmits them to a computer for calculating leak source location.

Based on the digital twin, a simulation model of a magnesium-aluminum alloy flat plate with a length and width of 1 m×1 m and a thickness of 2.5 mm is established according to the experimental platform. A cylindrical through-hole with a hole diameter of 1mm is also established in the flat plate to simulate the leakage point. When the leak occurs, the air pressure difference between the two sides of the leak will make the gas flow through the leak, thus it generates a pressure on the wall around the leak hole, which will form an elastic wave and propagate in the wall according to the solid mechanics theory. Meanwhile, the wall of the leak hole has been subjected to the pressure from the gas leak, and this pressure value is always existed but unstable due to the turbulent jet formed by the high-speed flow of gas. Based on the experimental results, the explosion model is used to simulate the pressure on the wall around the leak hole. A transient solver is established, and the stress tensor (N/m^2) distribution field of the elastic wave in the z-direction is calculated as shown in Fig. 10 (after 0.01 s of leak excitation).

According to the piezoelectric effect, the output voltage V of the piezoelectric sensor can be expressed by the relationship between the external pressure F, the piezoelectric constant g_{33}, the thickness h and the cross-sectional area A of the piezoelectric material element.

$$V = \frac{F \times g_{33} \times h}{A} \tag{20}$$

Based on the parameters of Nano30 sensor, the simulation data which is acquired by the sensor is calculated by (20). In order to verify the rationality of simulation data, the measurement results and the simulation results under the same conditions are selected, as shown in Fig. 11.

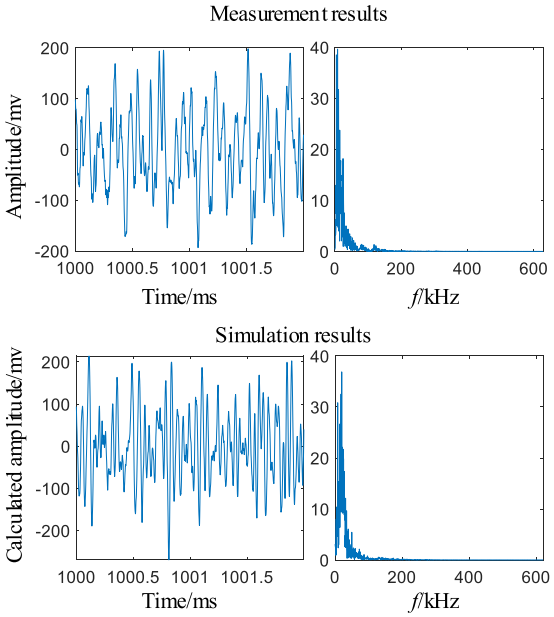

FIGURE 11. Experimental results and simulation results under the same conditions.

Fig. 11 depicts that the simulation data and the experimental data have similar properties (amplitude range, frequency distribution, etc.) in the time-frequency domain, thus the simulation data is reasonable. According to Fig. 8, the samples under different R are obtained by changing the position of the leakage hole and the position of the acquisition points. The data are preprocessed according to (12), and the training data set with labels (R) is constructed for training the deep learning model proposed in this paper.

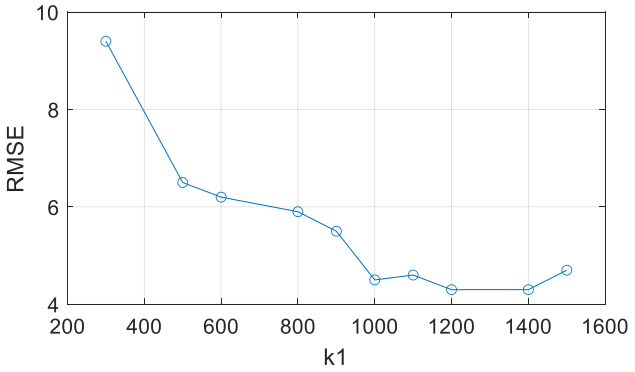

FIGURE 12. Relationship between the number of data samples (time domain) and RMSE.

B. KEY PARAMETERS OF THE DEEP LEARNING MODEL

According to Fig.7, the four parameters k_1, k_2, P_1, P_2 need to be determined for deep learning model to obtain the most accurate R. In accordance with the actual hardware limitations, take $a = 8$mm, sampling rate is 3MHz. The optimizer selects SGDM (stochastic gradient descent with momentum), the initial learning rate is set to 0.01, and the learning rate drops to 0.75 times of the original after 5 epochs, and the max epochs is 30.

1) NUMBER OF SAMPLES OF THE DATA SET IN THE TIME DOMAIN

Let $k_2 = 8$, $P_1 = P_2 = 4$, the value of k_1 is taken to increase sequentially from 300 to 1500, then the model performance is discussed for different sampling number conditions. The RMSE is selected as the evaluation index. Based on mean value of multiple results, the summary data are shown in Fig. 12.

As shown in Fig. 12, the RMSE of the model is small and changes stably when $k_1 \geqslant 1000$, in other words, the calculating accuracy of the model for R is higher within this range. Considering the complexity of the model increases rapidly with the increase of k_1, in practical application, $k_1 = 1000$ is used.

2) NUMBER OF SAMPLES OF THE DATA SET IN THE SPATIAL DOMAIN

According to the conclusion of the previous section, let $k_1 = 1000$, $P_1 = P_2 = 128$ (As a comparison term, $k_1 = 500$, $P_1 = P_2 = 64$), based on Fig. 2, different elements in the array are selected for the experiments($g = 4$), and the RMSE is selected to evaluate the model performance. Representative combinations of sensor arrays and their calculating results are summarized in Table 1 (mean value of the results of the three experiments).

According to Table 1, the model training results become better with the increase of the number of sensors in the array, and the model performs best when $k_2 = 8$ (RMSE = 0.9). Also, a similar conclusion exists when $k_1 = 500$.

TABLE 1. Results of different sensor array models.

The sensor No.	RMSE	
	k_1=1000	k_1=500
1368	5.6	11.3
1256	4.5	7.2
12468	3.2	7.5
13457	3.9	7.3
123567	1.2	4.1
12345678	0.9	3.1
123456789	1	3.5
12345678910	1.2	3.5

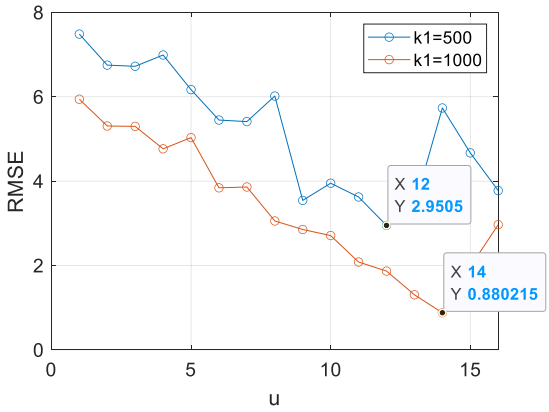

FIGURE 13. Relationship between the convolutional layer size and RMSE.

3) CONVOLUTIONAL LAYER SIZE

Once the Spatio-temporal size of the dataset is determined, the size of the convolutional layers in the model is discussed in this section. According to the conclusion of the previous sections,let $k_1 = 1000$(As a comparison term, $k_1 = 500$), $k_2 = 8$, $\mathbf{P} = [P_1, P_2] = [4, 4; 4, 8; 8, 8; 8, 16; pu; \ldots; 256, 256]$. The results of models with different convolutional kernel are summarized in Fig. 13. All experimental results are averaged over 3 times of data.

As shown in Fig. 13, $k_1 = 500$ and $k_1 = 1000$, the minimum values at different $\mathbf{P}$ could be obtained. When $u = 12$ ($P_1 = P_2 = 128$), the model with $k_1 = 500$ has the smallest RMSE (2.95); when $u = 14$ ($P_1 = P_2 = 256$) the model with $k_1 = 1000$ has the smallest RMSE (0.8802). According to the experimental statistical results, the model has the highest accuracy in calculating the distance when the convolution layer size is about 1/4 of the number of sampling points in the time domain.

C. MODEL TRAINING

The training data are obtained using finite element simulations and experiments, and the data are constructed according

TABLE 2. The main statistical characteristics of the data set.

The statistical properties	R	θ
Mean value	55 cm	45 °
Median value	55 cm	45 °
Range	70 cm	90 °
Mean deviation	17.624	21.32
Coefficient of variation	0.371	0.573
Kurtosis	-1.2	-1.03
Skewness	0	0.0096

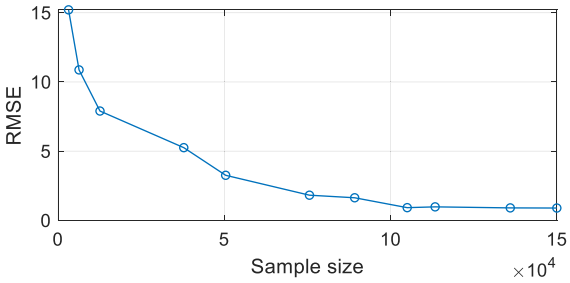

FIGURE 14. The actual values and calculated values of R for part of the test set.

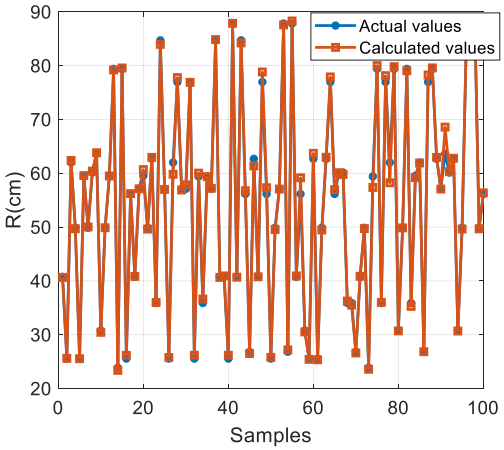

FIGURE 15. The actual values and calculated values of R for part of the validation set.

TABLE 3. The performance indicators of difrent networks.

	RMSE (cm)	MSE (cm)	MAE (cm)	R^2	NSE	RSR
RecCNN	0.920	0.846	0.398	0.988	0.921	0.038
LeNet-5	10.07	101.405	5.913	0.620	0.593	0.416
VGG-16	3.93	15.445	3.129	0.828	0.762	0.163

to the (12) to finally form the training data set for model training. In this paper, the distance R parameter involves the range of 20 cm -90 cm, the angle θ involves the range of 0 °-90 °. The main statistical characteristics of the data set based on the above two variables are shown in the Table 2.

Data sets containing different numbers of samples are constructed and trained, and the summary of RMSE is shown in Fig. 14. Where 70% of the samples in the data set are selected and imported into the network shown in Fig. 7 for training. 20% of the samples are used as the validation set to verify the results and 10% of the samples are used as the test set.

As show in Fig. 14, with the increase of the total number of samples, RMSE shows a rapid decline trend. while, when the total number of samples exceeded 100000, the trend became very slow. Considering the locating accuracy and system complexity, the total number of sample size is 105,000 in this paper. In this case, the confidence interval for the error estimation of R is $[-0.63,0.66]$ under the calculated confidence level is 95%. Some of the calculated results of validation set are shown in Fig. 15.

According to (14)-(19), the performance indicators of the network proposed in this paper (RecCNN) are calculated as shown in Table 3. Meanwhile, as a comparison, the results of the classical CNN model (LeNet-5 [33] and VGG-16 [34]) which added a regression layer to satisfy the regression calculation are calculated under the same data set.

The calculation results in Table 3 introduce that the RecCNN can fit the sample data well and obtain accurate distance prediction values. Compared with the other two networks, the RecCNN proposed in this paper has a smaller error and a higher degree of fitting. This is mainly because the data set is extremely asymmetric in the space and the time dimensions, and the rectangular convolution kernel is more conducive to feature extraction of this kind of data, which is suitable for engineering applications with unbalanced spatiotemporal sampling rate. At the same time, it can be seen that the deeper network will reduce the error to a certain extent, but the efficiency is poor.

IV. EXPERIMENTAL RESULTS AND DISCUSSION

In the test set, 70 groups of samples with different R values were selected for calculating, the data were summarized to analyze the R and θ errors and further calculate the locating errors. Using the actual distance R, the distance error ΔR and the angle error $\Delta\theta$ as the horizontal and vertical coordinates respectively, the error distribution is plotted as shown in Fig. 16.

Based on the data statistics, the maximum absolute value of ΔR is 0.82 cm, and the MAE (mean absolute error) is 0.3751 cm, the RMSE is 0.4123 cm; for the angle error $\Delta\theta$, the maximum error is 0.9 °, and the mean absolute error is 0.3747 °. The locating error d can be calculated by ΔR, $\Delta\theta$, θ and R, thus the result is shown in Fig.17.

Fig. 17 depicts, the maximum locating error is 1.46 cm, and the mean locating error is 0.5633 cm. According to Fig. 16 and 17, it can be confirmed that, based on the simulation model, the network proposed in this paper has a good generalization ability. Besides, the probability of large errors in the calculation of R is extremely low, which can be eliminated by

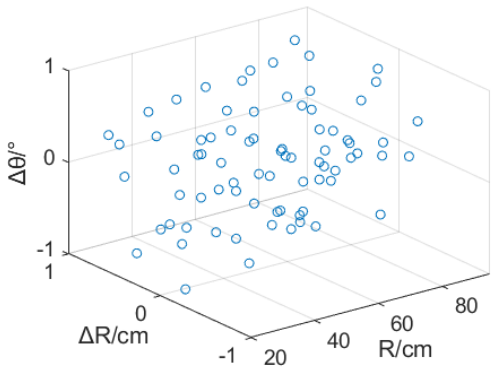

FIGURE 16. Distribution map of R-ΔR-Δθ.

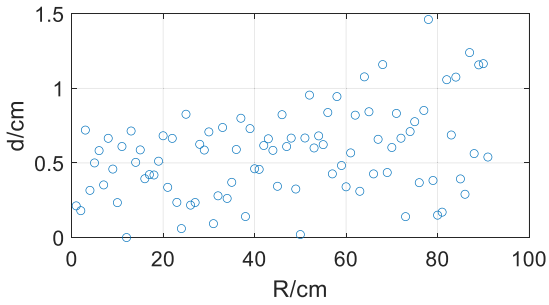

FIGURE 17. Locating error distribution chart.

voting the calculated values in multiple time periods (ensemble learning) or calculating the mean value.

The generalization ability of the model is further evaluated by using the data collected by the experimental platform as shown in Fig. 9. Taking an experimental result as an example, the coordinates of the leakage hole is (0,0) and the coordinates of the sensor array (element 1) is (30, −45), and the angle-energy relationship can be calculated according to (5)-(11). For the visual representation, the relationship is plotted as shown in Fig. 3. There is a unique and obvious energy peak when $\theta = 55$ °. According to (11), the angle corresponding to the peak is the one between the leakage source and the reference line of the sensor array. Simultaneously, 8 elements in the array to collect data are constructed according to (12) and sent to the trained model for calculating, furthermore, the result is 54.587 cm. A schematic diagram of the positioning is shown in Fig. 18. The error between the calculated result and the actual leak hole position ($R = 54.1$ cm, $\theta = 54.3$ °) is about 0.6 cm.

Further experiments are carried out on leakage holes at different positions in the test plate, and the calculation results at 5 different times are selected for statistics, which are summarized as shown in Table 4. Simulation experiment samples with the same leakage position are selected as the comparison group.

According to Table 4, compared with the simulation experimental group, the variance of R in the field experiment is larger, in other words, the calculation results are more

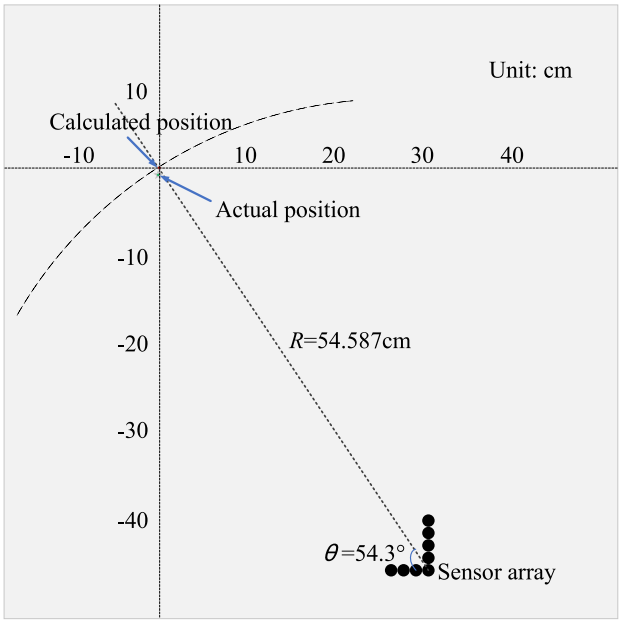

FIGURE 18. A schematic diagram of the locating.

TABLE 4. The experimental results with different leakage holes in the test plate.

No.	Actual value		Field experimental data		Finite element simulation data	
			Mean	var	Mean	var
1	R/cm	21.5	21.42	0.947	21.52	0.367
	θ/°	10	10.2	0.3	10.36	0.308
2	R/cm	34.9	34.58	2.867	35.1	0.18
	θ/°	55	55.16	0.428	55.12	0.132
3	R/cm	43.1	43.6	1.38	43.36	0.263
	θ/°	5.5	6.16	0.488	5.24	0.388
4	R/cm	54.1	54.62	1.717	54.28	0.327
	θ/°	55	55.2	0.1	55.2	0.18
5	R/cm	68.5	68.5	1.745	68.4	0.34
	θ/°	23	23.08	0.272	23.08	0.412
6	R/cm	72.3	72.06	4.353	72.18	0.787
	θ/°	72	71.92	0.052	72.28	0.372
7	R/cm	88.2	88.58	2.747	88.64	1.023
	θ/°	45	44.96	0.028	45.12	0.092

unstable and the error of single calculation results is larger. However, there is no significant difference in the statistical results of mean value. In summary, although the finite element simulation model cannot perfectly simulate the field experiment, there still exits errors between the simulated elastic wave data excited by leakage in the wall and the actual

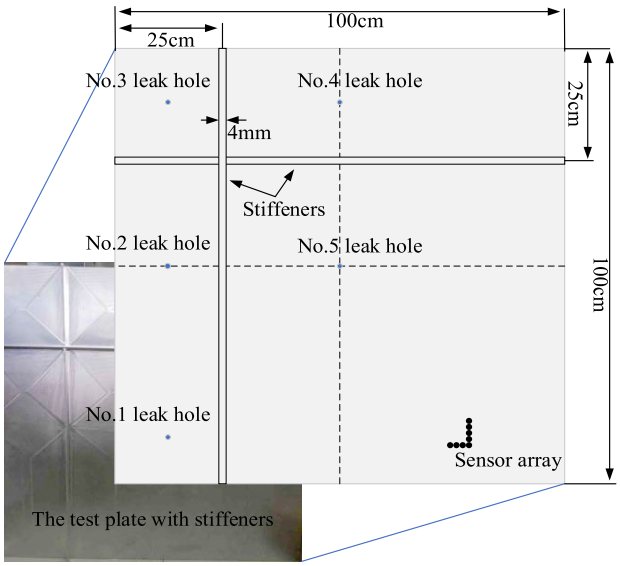

FIGURE 19. The test plate with stiffeners.

TABLE 5. The distance r calculated on the stiffener test plate.

No.	Actual value of R(cm)	Present network		Retrained network based on new test plate	
		Mean/cm	var	Mean/cm	var
1	87.5	82.6	60.46	87.7	2.233
2	81	82.1	66.64	81.7	1.322
3	67.5	64.7	21.67	68.1	0.965
4	87.1	77.8	32.33	88	1.858
5	54.6	60.3	55.73	54.4	2.195

data. Nevertheless, the statistical data show that the network established in this paper has good generalization ability, and the leak location method based on the network can meet the requirements of the field experiment platform. Meanwhile, according to statistics, the single locating time is less than 2 s, which can meet the real-time requirements in most application scenarios. Compared with the existing technology, on the one hand, the locating which was realized by multi-sensor array can be reduced to a single sensor, moreover the system complexity is also reduced. On the other hand, the method can locate the leak source at any time after the leak occurs, which greatly expands the application scope of the method.

In order to detect the generalization ability of the network which is different from the training scenarios, according to the test plate in Fig. 9, a new test plate with stiffener (4 mm wide and 20 mm high) is processed as shown in Fig. 19, on the basis of other parameters remaining unchanged.

Experiments are carried out on 5 leakage holes with 1mm aperture at different positions in the test plate. And the coordinate of the sensor array is (30, −45). The experimental results are summarized in Table 5.

According to Table 5, based on the present network, the error between the calculated value and the real value of R increases. Meanwhile, the calculated results of R have a large deviation from the actual value, and the variance of multiple experimental results is large. Therefore, the calculated results are unstable. The experimental results show that the wall structure has the influence on the generalization ability of the network. In order to obtain more accurate localization results, the network needs to be retrained according to the new structure when the wall structure changes greatly.

V. CONCLUSION

In this paper, a new method for real-time localization of large pressure vessel leak sources were designed and implemented by establishing a convolutional neural network based on elastic wavefield images. After analyzing the theoretical and experimental results, the conclusions are summarized as follows.

This study has identified that the spatial distribution of elastic wave field excited by the leakage source in the wall is closely related to the location of the leakage source. When the location of leakage source changes, the distribution of elastic wave field in space also changes.

Experimental results show that the RecCNN proposed in this paper can fit the sample data well and obtain accurate distance prediction values, where RMSE = 0.92cm, MAE = 0.398 cm, R^2 = 0.988 and NSE = 0.921. Compared with classical convolutional neural networks, the RMSE is up to about 11 times lower, the MAE is up to about 14 times lower, the R^2 is up to about 59% higher and the NSE is up to about 55% higher.

These experiments confirmed that, when the structure of the wall changes significantly, the trained network has a certain generalization ability, whereas it will bring a large locating error, the maximum locating error is 12.52 cm. The proposed method can be used to retrain the network based on the new structure to obtain higher locating accuracy. After retrained network, the maximum locating error is 1.37 cm.

Experimental results show that the leak source location method proposed in this paper based on RecCNN and STCA has a maximum location error of 1.46 cm and an average location error of about 0.56 cm within the range of 1 m^2 test plate. Compared to traditional methods, this method significantly reduces the complexity of the system, allows and realizes real-time localization of the leak source using a single sensor array. At the same time, the amount of data needed to be processed on site is reduced, the applicability of the method is improved, and a new method is provided for real-time leak location of large pressure vessels such as spacecraft in orbit.

REFERENCES

[1] L. Solazzi and M. Vaccari, "Reliability design of a pressure vessel made of composite materials," *Compos. Struct.*, vol. 279, Jan. 2022, Art. no. 114726.

[2] M. A. Adegboye, W.-K. Fung, and A. Karnik, "Recent advances in pipeline monitoring and oil leakage detection technologies: Principles and approaches," *Sensors*, vol. 19, no. 11, p. 2548, Jun. 2019.

[3] S. I. Builo, "Acoustic-emission diagnostics of the effect of hydrogen on properties of materials," *Russian J. Nondestruct. Test.*, vol. 45, no. 11, pp. 818–821, Nov. 2009.
[4] P.-S. Murvay and I. Silea, "A survey on gas leak detection and localization techniques," *J. Loss Prevention Process Ind.*, vol. 25, no. 6, pp. 966–973, Nov. 2012.
[5] Y. C. Ma and Q. Chen, "Application of ultrasonic-based gas leak detection and location technology in manned spacecraft," *Instrum. Technol. Sensors*, vol. 11, pp. 341–343, Jan. 2009.
[6] D. Guo, Z. Cui, C. Liu, and Y. Li, "Analysis of the influencing factors of the leak detection method based on the disturbance-reflected signal," *Energies*, vol. 16, no. 2, p. 572, Jan. 2023.
[7] Y. Gao, F. Piltan, and J.-M. Kim, "A hybrid leak localization approach using acoustic emission for industrial pipelines," *Sensors*, vol. 22, no. 10, p. 3963, May 2022.
[8] S. L. M. R. Filho, J. A. de Oliveira, C. H. Lauro, and L. C. Brandão, "Monitoring of microturning process using acoustic emission signals," *J. Brazilian Soc. Mech. Sci. Eng.*, vol. 41, no. 6, pp. 1–11, Jun. 2019.
[9] Y. Zhang, N. Shi, X. Rui, L. Qi, L. Xu, X. Li, X. Huang, and J. Li, "A 3D leakage monitoring method for pressure vessel based on region segmentation and time difference estimation," *Measurement*, vol. 203, Nov. 2022, Art. no. 111941.
[10] Z. Li, T. Sun, Y. Wang, Y. Liu, and X. Sun, "Spatio-temporal analysis of marine water quality data based on cross-recurrence plot (CRP) and cross-recurrence quantitative analysis (CRQA)," *Entropy*, vol. 25, no. 4, p. 689, Apr. 2023.
[11] R. S. Reusser, S. D. Holland, D. E. Chimenti, and R. A. Roberts, "Reflection and transmission of guided ultrasonic plate waves by vertical stiffeners," *J. Acoust. Soc. Amer.*, vol. 136, no. 1, pp. 170–182, Jul. 2014.
[12] X. Bian, Y. Zhang, Y. Li, X. Gong, and S. Jin, "A new method of using sensor arrays for gas leakage location based on correlation of the time-space domain of continuous ultrasound," *Sensors*, vol. 15, no. 4, pp. 8266–8283, Apr. 2015.
[13] B. Xu and Z. Yu, "Research on continuous leak location method based on acoustic sensor array," *J. Vibrat. Shock*, vol. 36, no. 6, pp. 134–139, Jul. 2017.
[14] G. W. Farnell and E. L. Adler, "Elastic wave propagation in thin layers," *Physical Acoustics*, vol. 9. Montreal, QC, Canada: McGill Univ., Department of Electrical Engineering, 2012, pp. 35–127.
[15] H. Niu, E. Reeves, and P. Gerstoft, "Source localization in an ocean waveguide using supervised machine learning," *J. Acoust. Soc. Amer.*, vol. 142, no. 3, pp. 1176–1188, Sep. 2017.
[16] H. I. Burgan, "Comparison of different ANN (FFBP, GRNN, RBF) algorithms and multiple linear regression for daily streamflow prediction in Kocasu River, Turkey," *Fresenius Environ. Bull.*, vol. 31, no. 5, pp. 4699–4708, Feb. 2022.
[17] M. A. Abdou, "Literature review: Efficient deep neural networks techniques for medical image analysis," *Neural Comput. Appl.*, vol. 34, no. 8, pp. 5791–5812, Feb. 2022.
[18] K. Bi, L. Xie, H. Zhang, X. Chen, X. Gu, and Q. Tian, "Accurate medium-range global weather forecasting with 3D neural networks," *Nature*, vol. 619, no. 7970, pp. 533–538, Jul. 2023.
[19] I. K. Deo and R. Jaiman, "Predicting waves in fluids with deep neural network," *Phys. Fluids*, vol. 34, no. 6, pp. 1–35, Jun. 2022.
[20] C. Spandonidis, P. Theodoropoulos, F. Giannopoulos, N. Galiatsatos, and A. Petsa, "Evaluation of deep learning approaches for oil & gas pipeline leak detection using wireless sensor networks," *Eng. Appl. Artif. Intell.*, vol. 113, Aug. 2022, Art. no. 104890.
[21] Q. Wu and C.-M. Lee, "A modified leakage localization method using multilayer perceptron neural networks in a pressurized gas pipe," *Appl. Sci.*, vol. 9, no. 9, p. 1954, May 2019.
[22] J. Ye and N. Toyama, "Automatic defect detection for ultrasonic wave propagation imaging method using spatio-temporal convolution neural networks," *Struct. Health Monitor.*, vol. 21, no. 6, pp. 2750–2767, Mar. 2022.
[23] X. Wang, M. Lin, J. Li, J. Tong, X. Huang, L. Liang, Z. Fan, and Y. Liu, "Ultrasonic guided wave imaging with deep learning: Applications in corrosion mapping," *Mech. Syst. Signal Process.*, vol. 169, Apr. 2022, Art. no. 108761.
[24] R. Cui, G. Azuara, F. Lanza di Scalea, and E. Barrera, "Damage imaging in skin-stringer composite aircraft panel by ultrasonic-guided waves using deep learning with convolutional neural network," *Struct. Health Monitor.*, vol. 21, no. 3, pp. 1123–1138, May 2022.
[25] H. Mahajan and S. Banerjee, "Acoustic emission source localisation for structural health monitoring of rail sections based on a deep learning approach," *Meas. Sci. Technol.*, vol. 34, no. 4, Jan. 2023, Art. no. 044010.
[26] H. Niu, Z. Gong, E. Ozanich, P. Gerstoft, H. Wang, and Z. Li, "Deep-learning source localization using multi-frequency magnitude-only data," *J. Acoust. Soc. Amer.*, vol. 146, no. 1, pp. 211–222, Jul. 2019.
[27] Y. Li, P. Zhou, Y. Zhuang, X. Wu, Y. Liu, X. Han, and G. Chen, "An improved gas leakage model and research on the leakage field strength characteristics of R290 in limited space," *Appl. Sci.*, vol. 12, no. 11, p. 5657, Jun. 2022.
[28] R. Xiao, Q. Hu, and J. Li, "Leak detection of gas pipelines using acoustic signals based on wavelet transform and support vector machine," *Measurement*, vol. 146, pp. 479–489, Nov. 2019.
[29] R. Gorgin, Y. Luo, and Z. Wu, "Environmental and operational conditions effects on Lamb wave based structural health monitoring systems: A review," *Ultrasonics*, vol. 105, Jul. 2020, Art. no. 106114.
[30] Z. Chen and P.-H. Ho, "Global-connected network with generalized ReLU activation," *Pattern Recognit.*, vol. 96, Dec. 2019, Art. no. 106961.
[31] N. Elizabeth Michael, M. Mishra, S. Hasan, and A. Al-Durra, "Short-term solar power predicting model based on multi-step CNN stacked LSTM technique," *Energies*, vol. 15, no. 6, p. 2150, Mar. 2022.
[32] R. Eccles, H. Zhang, D. Hamilton, R. Trancoso, and J. Syktus, "Impacts of climate change on nutrient and sediment loads from a subtropical catchment," *J. Environ. Manage.*, vol. 345, Nov. 2023, Art. no. 118738.
[33] G. Wei, G. Li, J. Zhao, and A. He, "Development of a LeNet-5 gas identification CNN structure for electronic noses," *Sensors*, vol. 19, no. 1, p. 217, Jan. 2019.
[34] S. Tammina, "Transfer learning using VGG-16 with deep convolutional neural network for classifying images," *Int. J. Sci. Res. Publications*, vol. 9, no. 10, pp. 143–150, Oct. 2019.

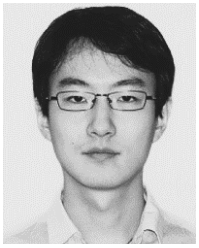

BIAN XU was born in Tianjin, China, in 1985. He received the Ph.D. degree in precision instruments and optoelectronics engineering from Tianjin University, Tianjin, in 2016.

Since 2019, he has been with the Renai College, Tianjin University, and continues his research work on real-time localization of pressure vessel leaks during the Ph.D. degree. He has been a Postdoctoral Researcher with the State Key Laboratory of Precision Measurement Technology and Instrument, Tianjin University, since 2022. He has published more than ten articles and applied for more than 20 inventions. His current research interests include the application of machine learning in non-destructive testing and high-precision sensor research.

Dr. Xu received the Third Prize of Scientific and Technological Progress of the Chinese *Journal of Instrumentation*, in 2022.

HUANG XINJING received the B.Sc. and Ph.D. degrees in instrument science and technology from Tianjin University, Tianjin, China, in 2010 and 2016, respectively.

In 2016, he joined the Modern Acoustic Testing Laboratory, Tianjin University, as an Assistant Professor. Since 2020, he has been an Associate Professor with the School of Precision Instrument and Opto-Electronics Engineering, Tianjin University. He is currently with the State Key Laboratory of Precision Measurement Technology and Instrument, Tianjin University. His current research interests include structural health inspection and/or monitoring technology, acoustic metamaterial devices and sensors, magnetic/acoustic sensing and measurement, and intelligent perception electronic systems.